Influence of aberrations in third harmonic generation microscopy

Anisha Thayil, Alexander Jesacher, Tony Wilson and Martin J. Booth

Department of Engineering Science, University of Oxford, Oxford OX1 3PJ, United Kingdom

E-mail: martin.booth@eng.ox.ac.uk

Abstract. We present an analysis of the effects of aberrations in third harmonic generation (THG) microscopy by considering different specimen geometries. Numerical simulations show the general trend that signal intensity and resolution are reduced as aberrations increase in amplitude. It is also shown that there are certain combinations of specimen structure and focusing position for which the presence of aberrations results in an increase in the image intensity. This occurs, for example, when there are several interfaces near the focal volume. The axial spreading of the excitation focal volume increases the characteristic coherence length for THG signal build up resulting in a significant contribution to the image brightness from axial planes near the focal plane. These results have important consequences for the interpretation of THG microscope images and for image based aberration correction in adaptive optics THG microscopy.

PACS numbers: 00.00, 20.00, 42.10

Keywords: aberrations, adaptive optics, harmonic generation, microscopy

1. Introduction

Third harmonic generation (THG) microscopy generates three dimensional images using the intrinsic optical properties of the specimen. This label-free imaging property makes THG microscopy an attractive tool for biological applications [1, 2, 3]. In THG microscopy, third harmonic light is generated at the focal point of a tightly focused ultrashort pulsed laser beam. Because of the coherent nature of the THG no net signal is obtained when focussed inside a homogeneous, normally dispersive medium. This is because of the Gouy phase shift experienced by the excitation beam near the focus [4]. However, when the nonlinear medium is not uniform, either in the refractive index or in the nonlinear susceptibility, the THG signal does not vanish, and significant THG output can be obtained [5]. This coherent nature of the THG process renders THG microscopy highly sensitive to inhomogeneities and the efficiency of signal generation strongly depends on the relative size of the inhomogeneity and the focal volume [6]. This specificity makes THG microscopy useful as a tool for material characterization [7, 8].

The performance of microscopes is often affected by aberrations, which may be caused by imperfections in the optical system or by the optical properties of the specimen [9]. These aberrations cause distortion of the focal spot leading to reduced focal intensity and resolution. Being a third-order nonlinear optical process, the THG signal level varies with the third power of incident illumination intensity. This makes THG microscopy particularly sensitive to the effects of aberrations. Furthermore, for THG imaging it is desirable to use near infrared excitation wavelengths around 1200nm, producing THG emission around 400nm [10]. This has two benefits: i) that the phototoxic effects of the illumination wavelength are reduced, compared to using shorter wavelengths, ii) that the emission occurs at wavelengths compatible with standard optics and detectors. However, as the illumination wavelength of 1200nm is usually outside the specification of most objective lenses, system aberrations can be significant.

The combination of system and specimen aberrations in THG microscopes can lead to a significant reduction in image quality. Similar problems in a number of microscope systems have been overcome using adaptive optics to correct aberrations [11]. These techniques were recently applied to harmonic generation microscopy [12, 13], where aberrations were corrected through optimisation of image-based quality metrics, such as image intensity. These optimisation methods are founded on the presumption that the maximum of the quality metric is coincident with optimal

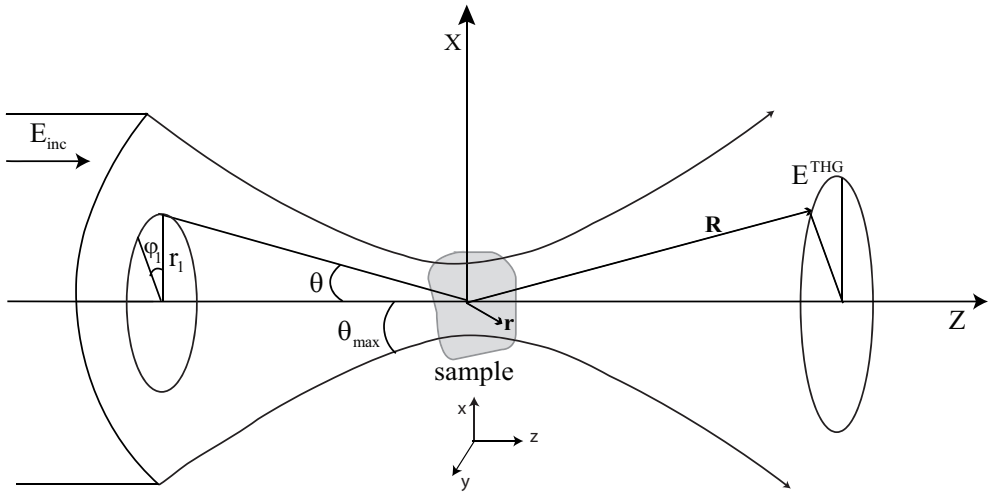

Figure 1. THG signal generation from a sample by a focussed laser beam and definition of the coordinate notations.

compensation of aberrations.

Here we analyse the influence of aberrations on THG signal from different specimen geometries such as interfaces, slabs, periodic structures and spheres. We demonstrate that the magnitude of THG signal and the THG response curves of these samples are strongly dependent on aberrations. In addition, we consider the implications of our results on an image intensity based aberration correction scheme in THG microscopy. We found that for some specific sample and focusing geometries, the maximum image intensity did not occur for zero aberration. We investigate how appropriate image averaging can help avoid this problem.

2. Theory

In this section we describe the theoretical procedure that was used to calculate THG response from different sample geometries for excitation fields with different aberrations. The focal field calculations are based on vectorial Debye theory for high NA focusing [14, 15] and the THG signal is estimated in the far-field using Green's function approach [16, 8]. Figure 1 shows a schematic diagram of the focusing geometry and the coordinate systems used.

We assumed a flat field distribution over the objective pupil plane. This assumption is motivated by the fact that in most experimental situations, especially when using high-NA objectives, the objective pupil plane is over illuminated. For

simplicity we assumed that the laser is linearly polarized along x direction and neglected any depolarization effects due to high NA focusing. It was shown by Olivier *et al.* [6] that the THG emission from simple interfaces excited by a focussed Gaussian beam can be adequately represented in this configuration by the x-polarised component alone, as the contributions from the y and z components to the total THG signal are minimal. The x polarized component of the unaberrated focal field is calculated using the expression,

$$E_f(r,\psi,z) = \frac{i}{\lambda}\int_0^{2\pi}\int_0^{\theta_{max}} p(r_1,\varphi_1)\sqrt{\cos\theta}[\cos\theta + \sin^2\varphi_1(1-\cos\theta)] \exp(-ik_1 r\sin\theta\cos(\varphi_1-\psi))\exp(-ik_1 z\cos\theta)\sin\theta d\theta d\varphi_1 \quad (1)$$

where λ is the wavelength and k_1 is the wave vector amplitude of the excitation field. $n_1\sin\theta_{max} = NA$ is the numerical aperture of the focusing objective where n_1 is the refractive index of the medium for the fundamental field. The pupil function, $p(r_1,\varphi_1)$ describes the complex field distribution in the pupil plane of the objective lens. It is defined in terms of a normalized radial co-ordinate r_1 such that the pupil has a radius equal to 1, where $r_1 = \sin\theta/\sin\theta_{max}$. The pupil function is a very useful way of representing aberrations introduced into the system. In an unaberrated system,the pupil function $p(r_1,\varphi_1) = 1$. When wavefront aberrations are present in the system, $p(r_1,\varphi_1)$ can be represented as

$$p(r_1,\varphi_1) = \exp[i\Phi(r_1,\varphi_1)] \quad (2)$$

where $\Phi(r_1,\varphi_1)$ describes the phase aberrations and we assume that no amplitude aberrations are present in the system. The phase function, $\Phi(r_1,\varphi_1)$ can be described as a series of Zernike polynomials $Z_j(r_1,\varphi_1)$ as

$$\Phi(r_1,\varphi_1) = \sum_j a_j Z_j(r_1,\varphi_1) \quad (3)$$

where a_j are the Zernike mode amplitudes. For the focal field simulations presented in this paper, we used three lower order Zernike aberration modes namely, astigmatism (Z_5), coma (Z_7) and first order spherical aberration (Z_{11}) which are defined as,

$$Z_5(r_1,\varphi_1) = \sqrt{6}r_1^2\cos(2\varphi_1) \quad (4)$$

$$Z_7(r_1,\varphi_1) = 2\sqrt{2}(3r_1^3 - 2r_1)\cos(\varphi_1) \quad (5)$$

$$Z_{11}(r_1,\varphi_1) = \sqrt{5}(6r_1^4 - 6r_1^2 + 1) \quad (6)$$

Here we employ the indexing scheme explained by Neil *et al.* [17].

Once the field distribution near the focus is known, the induced nonlinear polarization in the focal volume can be calculated for a given sample geometry. For an isotropic sample, the nonlinear polarization, $P^{(3\omega)}(\mathbf{r})$ at third harmonic frequency ω_3 is given by,

$$P^{(3\omega)}(\mathbf{r}) = \chi^{(3)}(\mathbf{r})E_f(\mathbf{r})E_f(\mathbf{r})E_f(\mathbf{r}) \tag{7}$$

where $\chi^{(3)}(\mathbf{r})$ is the third order susceptibility and $\mathbf{r}$ is the position vector in the focal region. The THG field generated from all positions $\mathbf{r}$ in the focal volume is then propagated to a position $\mathbf{R}$ in the collection optics aperture. This can be expressed as [16, 8],

$$\mathrm{E}^{(\mathrm{THG})}(\mathbf{R}) = \int_V \mathbf{P}^{(3\omega)}(\mathbf{r})\mathbf{G}(\mathbf{R}-\mathbf{r})dV \tag{8}$$

where V is the excitation volume and $\mathbf{G}$ is the far-field Green's function given by

$$\mathbf{G} = \frac{\exp(ik_3R)}{4\pi R}[\mathbf{I} - \mathbf{R}.\mathbf{r}/R^2] \tag{9}$$

where $k_3 = n_3\omega_3/c$ is the amplitude of the third harmonic wave vector, n_3 is the refractive index of the medium for the THG signal field and $\mathbf{I}$ is a 3×3 unit matrix. By integrating $|E^{(THG)}(\mathbf{R})|^2$ over the front aperture of the collecting objective, the total THG power emitted in the forward direction can be calculated.

For the simulations presented in this paper, we assumed that the samples are dielectric, non-birefringent, normally dispersive media ($3k_1 - k_3 \leq 0$), which is relevant to most biological samples. However, for simplicity, our calculations do not take into account of the group velocity dispersion of the ultrashort pulses. All calculations assume an excitation wavelength, $\lambda_1 = 1235$ nm corresponding to the output of a Cr:Forsterite laser and a focusing objective of NA = 1.15. We used the refractive index of fused silica, $n_1 = 1.4475$ at 1235 nm and $n_3 = 1.4686$ at 411 nm [18]. We assume that the samples are isotropic media made of two homogeneous regions with third order susceptibilities $\chi_1^{(3)} = 1$ and $\chi_2^{(3)} = 0$ in the case of interface and slab geometries. When there are inhomogeneities, such as an interface, near the focus THG emission can be observed and the amplitude of the emitted signal is proportional to $\chi_1^{(3)} - \chi_2^{(3)}$ [5]. Our choice of these particular values for $\chi_1^{(3)}$ and $\chi_2^{(3)}$ does not therefore limit the wider applicability of our conclusions regarding the effects of aberrations to other combination of materials. For axially periodic samples we assume a sinusoidal variation of $\chi^{(3)}$ along the beam propagation axis. The forward emitted THG power is calculated over a plane of area 5×5 cm^2 perpendicular to the optical axis located at Z=2 cm. This approximates the effect of using a high NA condenser to collect the THG emission in the forward direction.

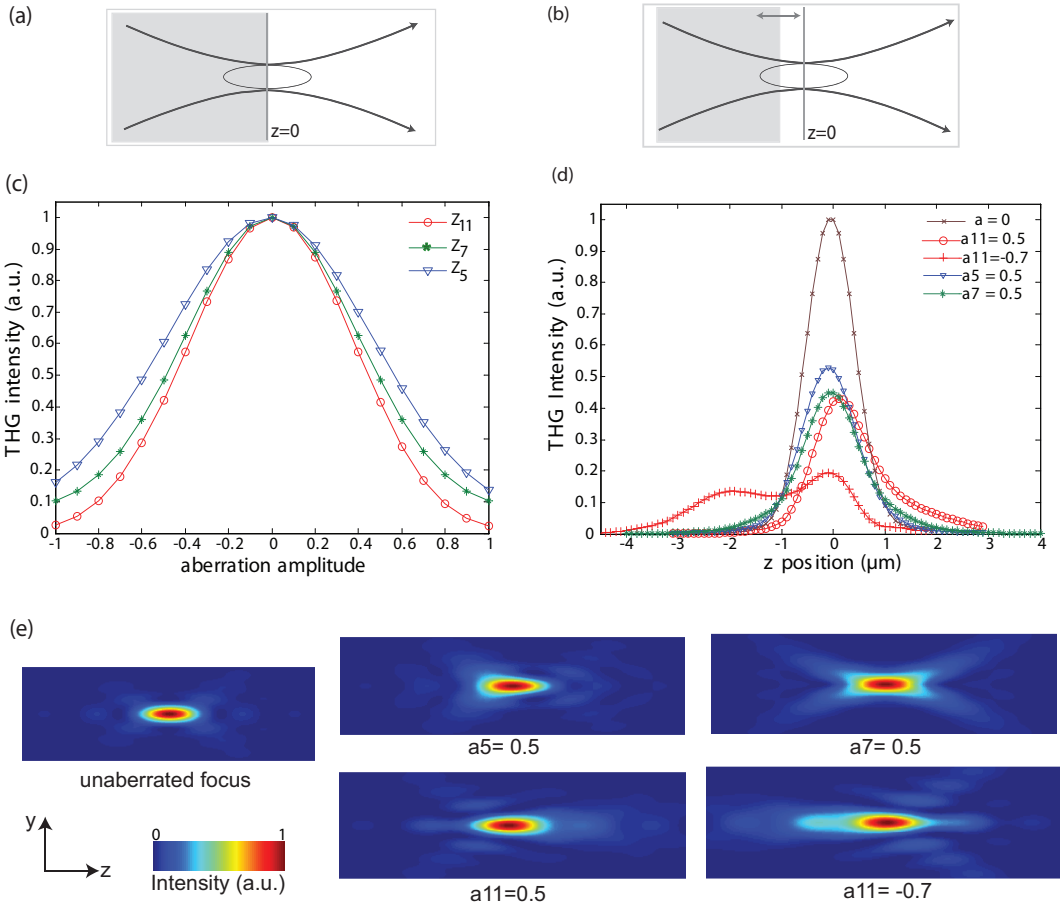

Figure 2. THG signal from an interface. (a)Schematic of the sample geometry. (b) Interface scanned along the optical axis.(c) THG signal as a function of Zernike aberration mode amplitudes, for astigmatism (Z_5), coma (Z_7) and first order spherical aberration (Z_{11}).(d) Axial intensity profiles of THG signal for different aberrations. (e) Normalized focal field intensity distribution in an axial plane along $x = 0$ corresponding to the different aberration modes considered in (d).

3. Results

3.1. THG from an interface

First we consider the case of an interface between two homogeneous, isotropic, semi-infinite media with different nonlinear susceptibility values $\chi_1^{(3)} = 1$ and $\chi_2^{(3)} = 0$, placed perpendicular to the excitation beam propagation. A schematic of the sample geometry is shown in figure 2(a). Here we assumed that the location of the focus is on

the interface. Figure 2(c) shows the total THG signal (corresponds to the integrated THG image intensity from the xy plane at z = 0) for different amplitudes of a given aberration mode. The coefficients a_5, a_7 and a_{11} denote the amplitudes of aberration modes Z_5, Z_7 and Z_{11} respectively. For each of these three aberration modes, the maximum THG signal corresponds to zero aberrations and there is a sharp decrease in the signal as aberration amplitudes are increased. This was expected because of the third order dependence of THG power on the excitation power. Although we have considered only three aberration modes, qualitatively similar behaviour is to be expected from any other modes. Figure 2(d) shows the THG signal variation as the interface is axially scanned across the focal volume. For the unaberrated case, the axial profile has a full width at half maximum (FWHM) of 1.15 μm, which corresponds to the optimum axial resolution of the microscope. By introducing an aberration amplitude of 0.5 as a representative case, we calculated the THG axial response corresponding to each of these three aberration modes. The excitation volume extends axially when aberrations are present in the system (figure 2(e)). This results in a wider THG axial profile. As reported by Pillai *et al* [19], presence of spherical aberration results in an asymmetric THG intensity profile in the axial direction. For larger a_{11} amplitudes, side peaks appear in the THG profile as shown in figure 2(d), where a_{11} was taken to be -0.7. For all the cases studied here, we found that dispersion reduces THG efficiency, but its relative effect on aberrated and unaberrated focal volumes remain the same (data not shown).

3.2. THG from a thin slab

Here we analyse the effect of aberrations on THG signal from an isotropic homogeneous thin slab placed perpendicular to the optical axis. d denotes the thickness of the slab in the axial direction and the slab is infinite in the transverse directions (figure 3(a)). We assumed that the slab has a different nonlinear susceptibility compared to the surrounding medium ($\chi_1^{(3)} = 1$ for the slab and $\chi_2^{(3)} = 0$ for the surrounding medium). Locating the focal spot at the middle of the sample, we simulated the far-field THG signal from slabs of different thickness. As shown in figures 3(b) and (c), for the unaberrated beam the THG signal from the slab peaks around $d = 0.8\mu m(\approx 0.7\lambda_1)$, which corresponds to the length over which coherent addition of THG signal field occurs [16]. When d is larger than 0.8μm, the phase mismatch introduced by the Gouy phase shift causes destructive interference of THG field from different parts of the sample. This decreases THG intensity and

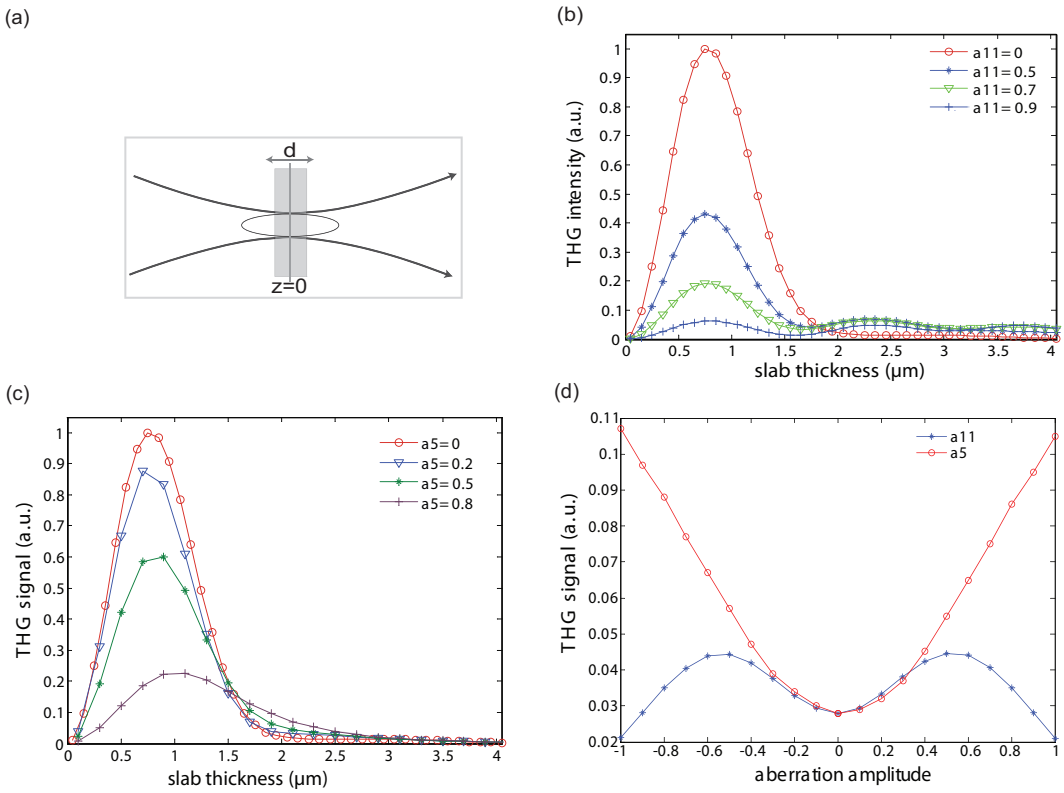

Figure 3. THG signal when focusing at the center of a thin slab. (a) Schematic of the sample geometry. (b)THG signal as a function of slab thickness for different amplitudes of Z_{11}.(c) THG response to slab thickness for different amount of Z_5. (d) THG signal from a slab of thickness, $d = 2\mu m$, for different amplitudes of Z_5 and Z_{11}

.

eventually no signal is obtained from the bulk of the medium. However, the presence of aberrations modify this behaviour. Figures 3(b) and (c) show THG response to slab thickness when aberrations are present in the system. Here we selected Z_5 and Z_{11} as two representative cases and for clarity of the graphs, we have shown the results from only 4 different aberration amplitudes. With the addition of a certain magnitude of Z_{11}, side peaks appear in the THG signal as the thickness of the slab is above the axial resolution limit. Presence of astigmatism increases the length over which the THG signal field interferes constructively and the signal falls off more slowly as slab thickness increases. Figure 3(d) shows variation of THG signal from a slab of thickness $d = 2\mu m$ with aberration amplitude. It should be noted that in

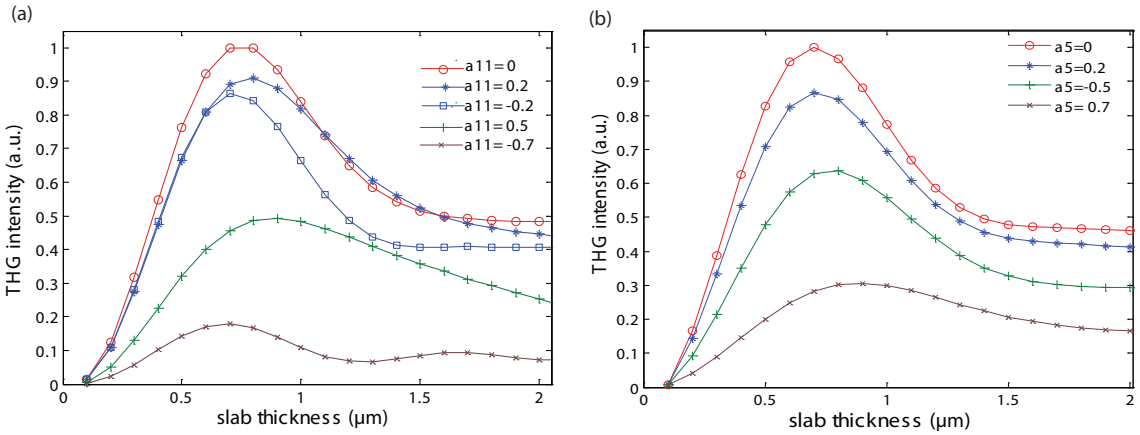

Figure 4. THG signal from a thin slab when focused at one of the interfaces. (a) THG signal as a function of slab thickness for different amplitudes of Z_{11}.(c) THG image intensity of the slab as the thickness varies, for different magnitudes of Z_5.

this case, maximum THG signal does not correspond to zero aberrations.

The axial location of the slab with respect to the point of maximum illumination intensity has significant effect on THG signal for different aberrations. We simulated the image intensity when focus is on one of the interfaces of the slab. THG signal for different amplitudes of Z_{11} and Z_5 are shown in figures 4(a) and (b) respectively. Depending on the sign of a_{11}, we notice a shift in the peak of the curve either to the lower or higher values of slab thickness . This is expected because of the axial asymmetry of the excitation field due to spherical aberration (see figure 2(e)). Interestingly for certain amplitudes of Z_{11}, the image intensity increases compared to the unaberrated case. As shown in figure 4(b), presence of astigmatism shifts the peak of the curve towards higher slab thickness. The sign of a_5 has no influence in the shape of the curve.

3.3. THG from a periodic sample

In what follows we describe the effect of spherical aberration on THG signal from an axially periodic sample. The sample is assumed to have a spatial variation of $\chi^{(3)}$, given by $\chi^{(3)} = 1 + \sin(2\pi z/e)/2$ where e denotes the axial period (figure 5(a)). Figure 5(b) shows the dependence of the THG signal on the axial period of the sample. The THG signal is maximum when $e = 1.8\mu m$ [6] for an unaberrated focus. Aberrations shift this peak of the curve and with larger amplitudes of Z_{11} side peaks appear. In addition, we notice that the THG efficiency falls off more slowly with e

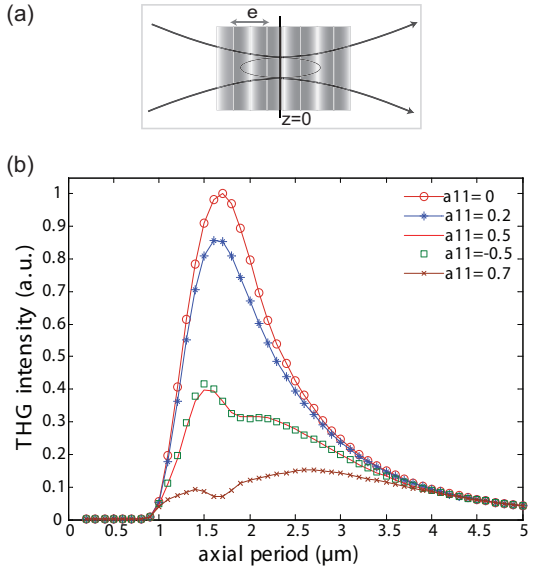

Figure 5. (a) Sample geometry. (b) Influence of spherical aberration on the THG signal from a periodic sample.

as the magnitude of a_{11} increases. Here the sign of a_{11} has no effect on the shape of the curve. It should be noted that for large spatial period of the sample, spherical aberration has no effect on the THG image brightness. The phase of the periodic structure at z = 0 can modulate the THG signal and therefore the results presented here need not be general for all relative positions of the structure and the illumination focus.

3.4. THG from a spherical sample

Next we compare THG signal from beads of different sizes for different amplitudes of spherical aberration. We assume that the sphere has a different nonlinear coefficient, $\chi^{(3)} = 1$ and the surrounding medium has $\chi^{(3)} = 0$. To simplify our simulations, we calculated the signal only from the center of each bead. This corresponds to the THG intensity of a single pixel at the centre of the bead. As expected, for smaller beads THG signal is reduced due to spherical aberration (figure 6(b)). As the bead diameter is increased, presence of spherical aberration result in a measurable signal from the center of the beads. Although, aberrations reduce the total THG signal from the beads, for certain focal positions, for example at the centre of the bead, aberrations may increase the measured THG signal.

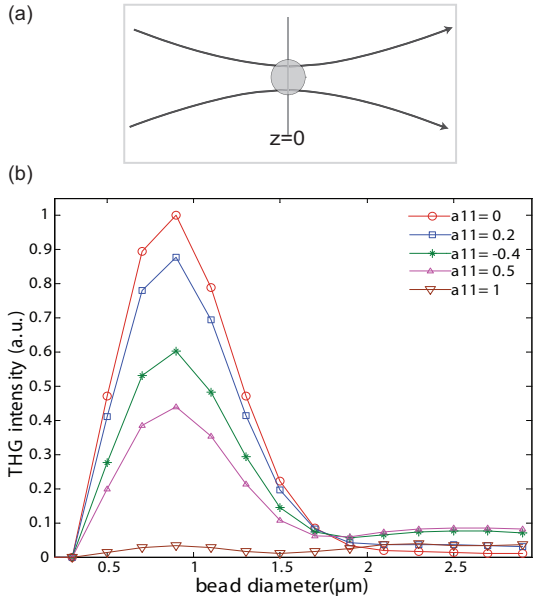

Figure 6. (a) Sample geometry (b) THG signal from beads of different diameters centred at the beam focus for different magnitudes of Z_{11}.

4. Discussion and Conclusions

The results from our simulations clearly show that the magnitude of the THG signal from different specimen geometries strongly depends on the presence of aberrations. Aberrations not only decrease the peak focal field intensity, but also cause elongation and distortion of the focal field distribution. These effects are clearly evident in the THG responses shown in the above section. For all the sample geometries considered here, the presence of aberrations results in a significant reduction in the overall THG signal and THG peak intensity. This significant intensity drop even with smaller aberration amplitudes is because of the third order dependence of the THG signal on the fundamental field. Apart from this, aberrations result in the axial spread of the THG response as shown in figure 1(d). As a consequence, the THG response curves are modified. For certain specific sample geometries and focusing positions, adding aberrations to the focal field result in an increase in the THG signal (figures 3, 4 and 6). This, in general, happens when the chosen focusing position in the sample is not the position of maximum THG signal. In some cases aberrations have no appreciable effect on the THG intensity (for example, for the larger spatial periods shown in figure 5b).

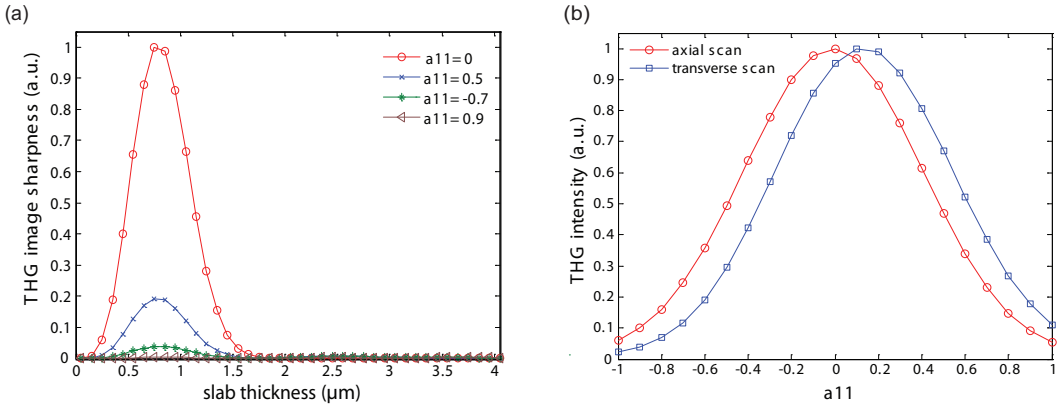

Figure 7. (a) Image sharpness for different amplitudes of Z_{11} as a function of slab thickness when focused at the middle of the slab. (b)Variation of THG image intensity of a thin slab of thickness 1.2 μm for different magnitudes of Z_{11}. The integrated intensity of the image from an axial plain (xz) peaks at zero aberrations whereas that of the image from a transverse plane (xy) perpendicular to one of the interfaces has a peak around $a_{11} = 0.2$

.

These results clearly indicate the importance of accounting for the effect of aberrations in THG microscopy particularly when it is used the for quantitative measurements of material parameters [19, 7]. Aberration correction in THG microscopes has been demonstrated using indirect, image based correction schemes [12, 13]. These schemes require selection of a suitable quality metric and it is assumed that the maximum of the metric correspond to zero aberrations. When image brightness is used as a quality metric, it is assumed that presence of aberrations cause a reduction in the image brightness. As evident from the above examples this assumption is not always valid. For some specific sample geometries and focusing positions, the total THG signal increases with aberrations. This in general happens when there are interfaces or other features near the focus. In such situations the chosen position does not correspond to the position of maximum THG signal from the sample. In certain situations, it has been suggested that using image sharpness (defined as the sum of the squared pixel values) could be a better choice of metric than total image intensity [13]. Figure 7(a) shows the variation of image sharpness with slab thickness for different amplitudes of Z_{11} (using the sample geometry depicted in figure 2(a)). Although this enhances stronger image signals, it does not remove the phenomenon that causes certain THG signals to increase when aberrations are

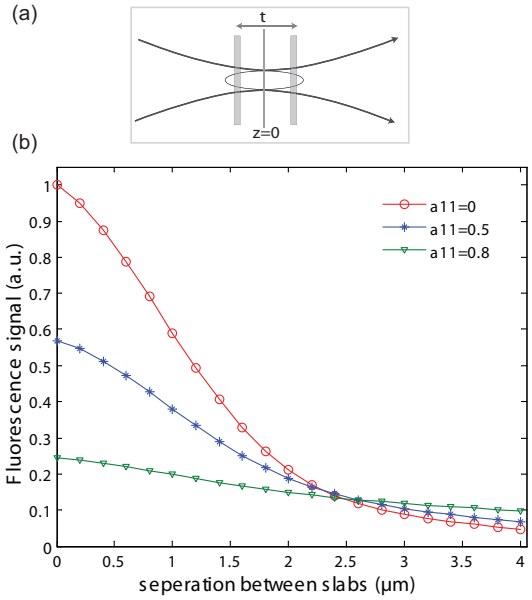

Figure 8. (a)Sample geometry. (b) Variation of two-photon fluorescence signal from the focal plane $z = 0$ as the separation between the two fluorescent slabs increases simulated for for different amplitudes of spherical aberration.

present. On the other hand, implementing a metric based on integrated image intensity (sum of pixel values taken from an xz, yz or volume scan) could be a better solution to overcome this problem. Figure 7(b) compares the total image intensity taken from an axial image plane through the slab of thickness $1.2\mu m$ and from a transverse image plane through one of the interfaces of the same slab as a function of a_{11}. Whilst the signal for the transverse scan does not peak at zero aberration, that from the axial scan does.

These phenomena are not confined to harmonic generation microscopy. Similar effects can also be observed in other forms of microscopes. For example in a confocal (or equivalently two-photon) fluorescence microscope, consider imaging two axially thin fluorescent layers separated by a distance larger than twice the diffraction-limited axial resolution of the microscope. When the focus is located between the layers, a negligible amount of fluorescence will be detected in a unaberrated system. However, when aberrations are added, the axial spreading of the PSF can lead to an increase in the detected signal at this point, even though the total detected signal drops (figure 8). Selecting this central plane for intensity optimisation will not result in the best aberration correction. This problem would be alleviated if the total image

intensity in an axially scanned plane encompassing both layers were used instead.

Acknowledgments

We acknowledge the support from the following grants: Biotechnology and Biological Science Research Council (BBE0049461), Engineering and Physical Sciences Research Council (EP/E055818/1) and Austrian Science Fund (J2826-N20).

References

[1] D. Yelin and Y. Silberberg, *Laser scanning third-harmonic-generation microscopy in biology*, Opt. Express **5**, 169 (1999).

[2] D. Debarre, W. Supatto, A.-M. Pena1, A. Fabre, T. Tordjmann, L. Combettes, M.-C. Schanne-Klein, and E. Beaurepaire, *Imaging lipid bodies in cells and tissues using third-harmonic generation microscopy*, Nat. Meth. **3**, 47 (2006).

[3] C.-S. Hsieh, S.-U. Chen, Y.-W. Lee, Y.-S. Yang, and C.-K. Sun, *Higher harmonic generation microscopy of in vitro cultured mammal oocytes and embryos*, Opt. Express **16**, 11574 (2008).

[4] R. W. Boyd, *Nonlinear Optics*, Academic Press, Academic Press, second edition, 2003.

[5] Y. Barad, H. Eisenberg, M. Horowitz, and Y. Silberberg, *Nonlinear scanning laser microscopy by third harmonic generation*, Appl. Phys. Lett. **70**, 922 (1997).

[6] N. Olivier and E. Beaurepaire, *Third-harmonic generation microscopy with focus-engineered beams: a numerical study*, Opt. Express **16**, 14703 (2008).

[7] J. M. Schins, T. Schrama, J. Squier, G. J. Brakenhoff, and M. Müller, *Determination of material properties by use of third-harmonic generation microscopy*, J. Opt. Soc. Am. B **19**, 1627 (2002).

[8] D. Débarre, N. Olivier, and E. Beaurepaire, *Signal epidetection in third-harmonic generation microscopy of turbid media*, Opt. Express **15**, 8913 (2007).

[9] M. Schwertner, M. Booth, and T. Wilson, *Characterizing specimen induced aberrations for high NA adaptive optical microscopy*, Opt. Express **12**, 6540 (2004).

[10] S.-W. Chu, I.-H. Chen, T.-M. Liu, P. C. Chen, C.-K. Sun, and B.-L. Lin, *Multimodal nonlinear spectral microscopy based on a femtosecond Cr:forsterite laser*, Opt. Lett. **26**, 1909 (2001).

[11] M. J.Booth, *Adaptive optics in microscopy*, Phil. Trans. R. Soc. A **365**, 2829 (2007).

[12] A. Jesacher, A. Thayil, K. Grieve, D. Débarre, T. Watanabe, T. Wilson, S. Srinivas, and M. Booth, *Adaptive harmonic generation microscopy of mammalian embryos*, Opt. Lett. **34**, 3154 (2009).

[13] N. Olivier, D. Débarre, and E. Beaurepaire, *Dynamic aberration correction for multiharmonic microscopy*, Opt. Lett. **34**, 3145 (2009).

[14] B. Richards and E. Wolf, *Electromagnetic Diffraction in Optical Systems. II. Structure of the Image Field in an Aplanatic System*, Proc. R. Soc. Lond. A **253**, 358379 (1959).

[15] M. Gu, *Advanced Opticsl Imaging Theory*, Springer-Verlag, Berlin Heidelberg Germany, 1999.

[16] J.-X. Cheng and X. S. Xie, *Green's function formulation for third-harmonic generation microscopy*, J. Opt. Soc. Am. B **19**, 1604 (2002).

[17] M. A. A. Neil, M. J. Booth, and T. Wilson, *New modal wave-front sensor: a theoretical analysis*, J. Opt. Soc. Am. A **17**, 1098 (2000).

[18] I. H. Malitson, *Interspecimen Comparison of the Refractive Index of Fused Silica*, J. Opt. Soc. Am. **55**, 1205 (1965).

[19] R. S. Pillai, G. J. Brakenhoff, and M. Müller, *Analysis of the influence of spherical aberration from focusing through a dielectric slab in quantitative nonlinear optical susceptibility measurements using third-harmonic generation*, Opt. Express **14**, 260 (2006).